DEEP REINFORCEMENT LEARNING FOR AEROSERVOELASTIC CONTROL OF UNMANNED MULTI-BODY AIRCRAFT WITH GEOMETRIC NONLINEARITIES

Ying Zhuolin[1, 2, 3, 4], Bi Ying[1, *], Zhu Zijian[1], Zhu Chen[1], Ma Xiaoping[1]

[1, *] Institute of Engineering Thermophysics, Chinese Academy of Sciences, Beijing, 100190, China;

[2] School of Aeronautics and Astronautics, University of Chinese Academy of Sciences, Beijing,

100049, China;

[3] National Key Laboratory of Science and Technology on Advanced Light-Duty Gas-Turbine, Beijing, 100049, China;

[4] Key Laboratory of UAV Emergency, Rescue Technology, Ministry of Emergency Management, Beijing, 102202, China

Keywords: Aeroservoelasticity, Large aspect ratio, Geometric nonlinearity, Gust alleviation

Abstract: This study explores the unique challenges posed by High Altitude Long Endurance (HALE) aircraft, focusing on their extreme flexibility. It investigates the significant deformations experienced by the lightweight and highly flexible wings during flight. To address issues like differential drag during takeoff and landing, an innovative solution - a Multi-Body Aircraft (MBA) design with wingtip docking capability - is introduced. However, multiple wingtip dockings introduce inevitable geometric nonlinearities, significantly affecting the aircraft's aeroelastic design. Aeroservoelastic analysis of unmanned multi-body aircraft considering geometric nonlinearities is urgently needed. The research develops a nonlinear finite element model and proposes control laws combining Deep Q Network and LQR control to effectively suppress gust responses, enhancing overall flight stability. This exploration provides valuable insights into the dynamics of flexible unmanned multi-body aircraft.

1   INTRODUCTION

In recent years, there has been a growing interest in the development of highly flexible Unmanned Aerial Vehicles (UAVs). Represented by High Altitude Long Endurance (HALE) aircraft, these aircraft typically feature lightweight and high flexibility characteristics. During flight, the significant structural deformation caused by their flexibility often results in nonlinear behavior of structural stiffness due to variations in geometric stiffness. In such cases, traditional linear theories and methods based on small deformation assumptions used in aeroelastic and flight dynamics analyses struggle to meet accuracy requirements and are no longer applicable[1]. The extreme length and low stiffness of flexible wings result in their natural vibration frequencies being of the same order of magnitude as the flight dynamic frequencies, leading to instability due to the interaction between flight dynamics and structural vibration[2].

Simultaneously, significant elastic deformation of the wings alters the aerodynamic configuration and stiffness characteristics of the aircraft, making the aeroelastic behavior significantly different under nonlinear conditions, thereby complicating the aeroelastic issues of highly flexible aircraft. Additionally, High Altitude Long Endurance UAVs typically employ modern fiber composite materials such as commonly used carbon fiber to reduce weight. However, these materials have relatively poor tolerance to compression stress, limiting the degree of wing bending and resulting in insufficient robustness of the aircraft's flight envelope. Therefore, structural failure incidents during flight testing have become one of the challenges faced by such UAVs.

In contrast, the unmanned multi-body aircraft (MBA) possess certain advantages in flexibility: flexibility is mainly concentrated in the connecting parts, while the wings have relatively high stiffness, reducing the impact on wing performance. Moreover, the unmanned multi-body aircraft (MBA), composed of multiple bodies, have more control surfaces, allowing for effective adjustment of flight attitude. Attitude changes are localized, and the effects of sudden disturbances on flight attitude are mitigated by the long-scale fuselage transmission.

Montalvo et al.[3–5] conducted in-depth research and analysis on the dynamic characteristics of various variants of Meta Aircraft using the Newton-Euler method and nonlinear lift line model. Kothe et al.[6], based on the Kane method, successfully constructed multi-body dynamic models of morphing aircraft and conducted closed-loop flight tests. Reference[7], based on the Newton-Euler equations and lift line method, established a multi-body UAV flight dynamics model represented by a twin-engine combination, analyzed its trim state and stability, and designed a stability augmentation control system using PID control methods, obtaining satisfactory simulation results. An Chao et al.[8] proposed a dynamic modeling method for multi-body aircraft, using the state-space vortex lattice method (VLM) to calculate aerodynamic coefficients, and obtaining the flight dynamics model in the absolute coordinate system based on the Newton-Euler equations, and conducted trim and stability analysis based on the dynamic model.

It is evident that existing research on hybrid aircraft mainly focuses on rigid body dynamics, with very little research on Aeroservoelastic analysis. As the importance of control systems in aircraft design continues to increase, Aeroservoelastic analysis has become an unavoidable analytical process. Hashemi et al.[9,10] proposed a control design for flexible wing aircraft, using wing root bending moment to measure gust load and optimize performance cost functions to minimize gust-induced loads, they found that the Basic Multi-Objective (BMO) controller performed the best, exhibiting the maximum stability margin. Wang et al.[11] proposed an incremental nonlinear dynamic inversion control method for flexible aircraft, which can alleviate gust loads and demonstrate inherent robustness to model uncertainties, external disturbances, and actuator failures through simulation and Monte Carlo studies. Downs and Prazenica[12] studied adaptive control of flexible wings, considering factors such as nonlinear structural stiffness and actuator backlash. The study showed that direct adaptive control strategies can improve the suppression effect of linear aeroelastic models under different flight conditions, especially performing well beyond flutter speed. Zhou et al.[13] proposed an intelligent neural network-based feedforward gust alleviation framework, forming a neural network training dataset by collecting flight data and gust data encountered during aircraft flight, training the neural network recognition model to accurately predict aircraft output, and then learning the parameters of the time-delay neural network controller based on the output of the recognition model and collected flight data. Simulation results showed that the intelligent controller had good gust alleviation effects for both continuous turbulence excitation and discrete gust excitation.

This paper conducts nonlinear Aeroservoelastic analysis and control research on a dual-body composite unmanned multi-body aircraft connected at the wingtips. By using the minimal state method for reasonable aerodynamic approximations, it comprehensively explores the coupling issues caused by geometric nonlinearity and aeroelasticity in the time domain. Additionally, a control method combining Deep Q Network and LQR controller is designed to achieve gust alleviation. The research results show that considering geometric nonlinearity, the proposed control law effectively reduces gust response, providing strong support for improving the overall flight stability of flexible multi-body UAVs. This comprehensive exploration provides valuable insights into the complex dynamics of flexible unmanned multi-body aircraft.

2 MODEL DESCRIPTION

The large aspect ratio composite aircraft single finite element model used in this study is shown in Figure 1. This model is analyzed using MSC/NASTRAN software and employs beam elements for simplified modeling, reducing computational cost while ensuring the accuracy and reliability of the simulation results. The model includes detailed structures of the wing, main wing spar, and control surfaces. This aircraft adopts a tailless configuration, featuring a simple structural design. The structural model is simplified to a straight wing with a wingspan of 1.96 meters and an aerodynamic chord length of 0.1 meters. The total weight of the aircraft is 1.302 kg. Additionally, the wing aspect ratio is 19.6, classifying it as a large aspect ratio aircraft. The main wing spar is made of high-strength aluminum alloy and serves as the primary load-bearing component. The aircraft is equipped with two independently controllable control surfaces. These control surfaces are driven by servo motors, enabling precise attitude control and aerodynamic adjustment.
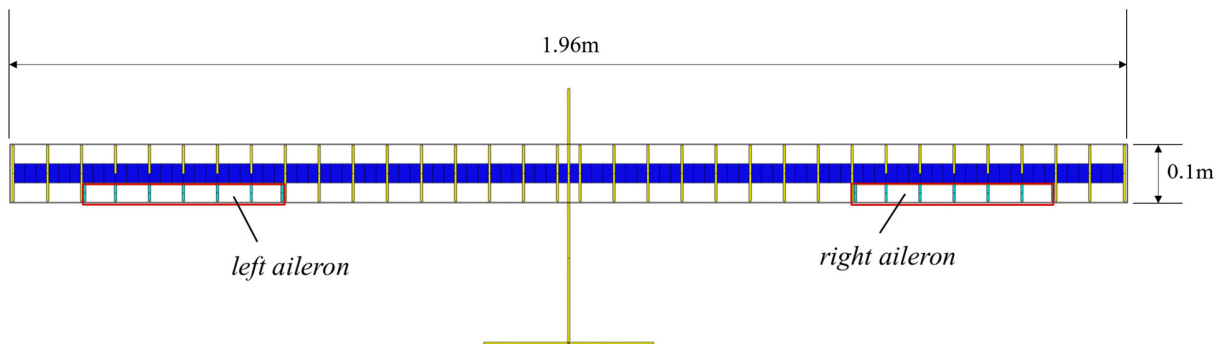

Figure 1 Sketch map of wing parameters of the single unmanned MBA

Table 1 Modal parameters of unmanned MBA

Parameters	Values	Parameters	Values
Span Length/ m	1.960	Position of Main Beam	50% Chord Length
Chord Length/ m	0.100	Modulus of Elasticity of Main Beam/ GPa	395.1
Structural mass/ kg	1.302	Cross-section Size of Main Beam/ m	0.035×0.0015

The connected composite aircraft model is shown in Figure 2. The connection is modeled after a hinged connection configuration with a width set to 0.04m. During finite element modeling, RBE2 elements and spring elements are primarily used for simulation.
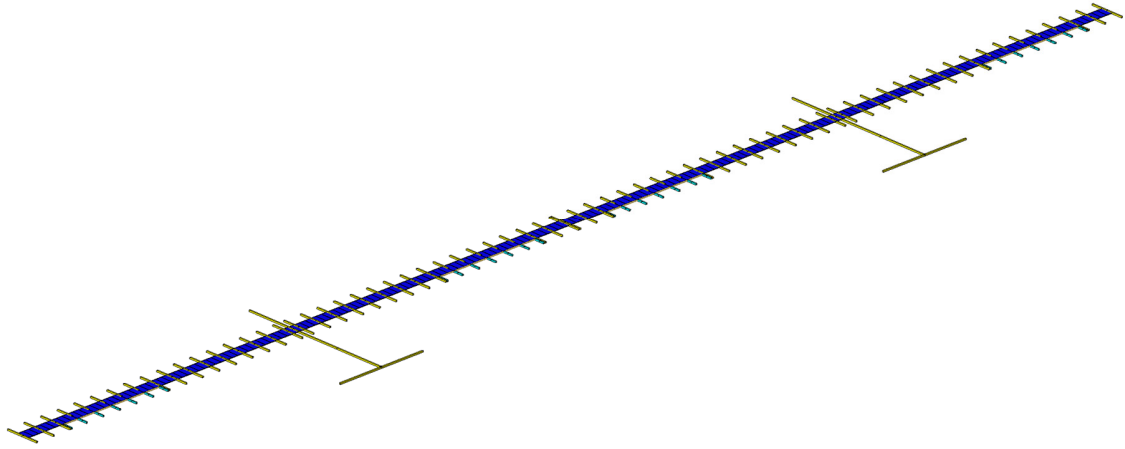
Figure 2 Model of docking two aircraft

The structural dynamic characteristics of the aircraft are analyzed using MSC/NASTRAN software, with the results shown below. Figure 3 and Figure 4 illustrate the main elastic mode shapes of the single and dual aircraft configurations. These modes include the primary bending and torsional modes of the wing, corresponding to the main deformation patterns of the wing. It is important to note that in-plane modes contribute negligibly to flutter and are therefore omitted in the analysis.
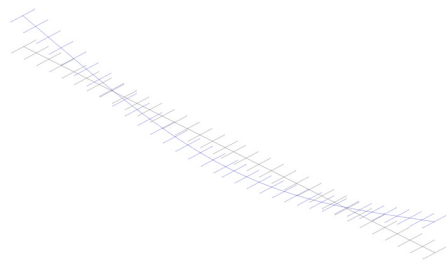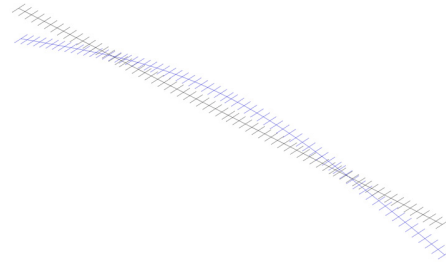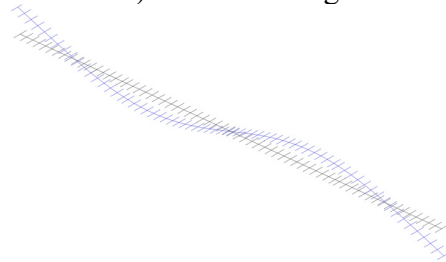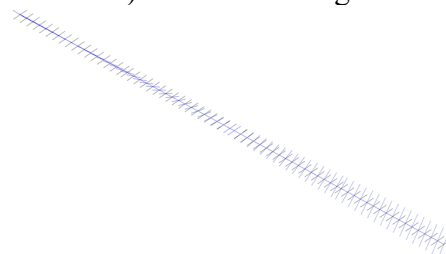

a) First Bending

a) First Bending
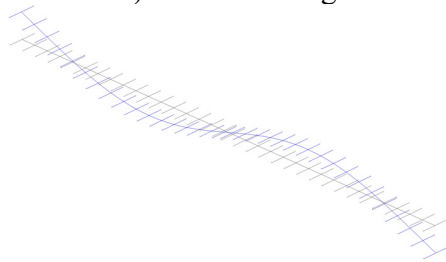
b) Second Bending
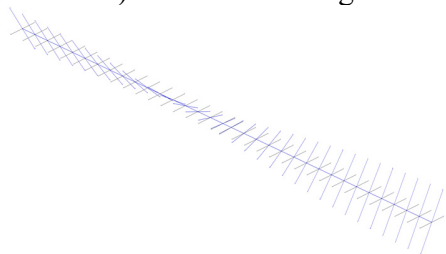
b) Second Bending

c) First Torsion
Figure 3 Single Aircraft

c) First Torsion
Figure 4 Dual Aircraft

Table 2 Major Modal Frequencies

Parameters	Single Aircraft		Dual Aircraft	
	Order	Frequency (Hz)	Order	Frequency (Hz)
First Bending	7	2.312	7	0.583
Second Bending	8	6.385	8	1.577
First Torsion	13	46.57	17	23.441

3 METHODOLOGIES

3.1 Integration of Deep Q-Network and Linear Quadratic Regulator

In the control of gust alleviation for flexible aircraft, a method combining Deep Q-Network (DQN) and Linear Quadratic Regulator (LQR) is employed to achieve effective control strategies.

First, the environment consists of the flexible aircraft model, gust disturbance model, and system state information. The flexible aircraft model describes the aircraft's dynamics and structural characteristics, while the gust disturbance model simulates the gust disturbances in the environment. The system state information includes the current state of the aircraft, such as wingtip acceleration. The primary function of the environment is to receive actions from the controller and compute the next state and reward based on the model.

The state information encompasses the current state of the flexible aircraft, such as wingtip acceleration, and these states are encoded as inputs to the neural network. Actions are control signals output by the LQR controller to regulate the actuators of the flexible aircraft, such as control surface deflection angles. These actions are encoded as outputs of the neural network.

The reward function is defined based on control performance and system state, guiding the DQN to learn the optimal control strategy. To incentivize the system to reduce vibration amplitude, the reward can be designed such that the smaller the vibration amplitude, the greater the reward.

The DQN consists of multiple neural network layers and is used to learn the value function of state-action pairs. The input to the network is the state, and the output is the Q-value for each action, representing the expected return of choosing that action in that state. To stabilize the training process and avoid overfitting, DQN employs experience replay and a target network. Experience replay is used to store experiences of states, actions, rewards, and next states encountered in the environment. By randomly sampling these experiences to train the DQN, it breaks the correlation between data and improves learning efficiency. The target network is used to compute the target Q-value, which is the maximum Q-value of the next state, as the target for training the DQN. The weights of the target network are a delayed version of the DQN weights, ensuring training stability.
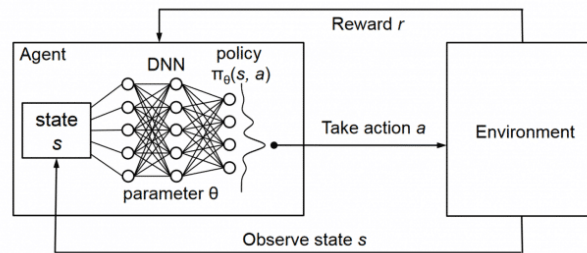

Figure 5 Deep Q Network Diagram

In terms of control strategy, based on the LQR principle, the control strategy learned by the DQN is used to compute the LQR gain matrix. Specifically, the LQR gain matrix is calculated based on the strategy learned by the DQN, and then control signals are output based on the current state and gain matrix to regulate the actuators of the flexible aircraft.

During the training process, the DQN continuously acquires experience data from the environment and trains the deep Q-network through the experience replay mechanism to learn the optimal control strategy. The learned control strategy is converted into parameters for the LQR controller, which is used to control the flexible aircraft in practice.

This method, which combines DQN and LQR, achieves effective control of the flexible aircraft under gust disturbances through the integration of deep learning and classical control theory. The DQN is responsible for learning the optimal control strategy, while the LQR uses this strategy to compute control signals, thereby adjusting the aircraft's actuators in different states to ultimately alleviate gust disturbances.

3.2 Control systems modeling

3.2.1 Aerodynamic Modeling

According to the frequency domain aerodynamic theory, the generalized unsteady aerodynamic force can be expressed as:

$$\mathbf{\Phi}\Delta\mathbf{f}_A = q_\infty \mathbf{Q}(ik) \begin{Bmatrix} \mathbf{q}_e \\ \mathbf{\delta} \\ \mathbf{w}_g \end{Bmatrix} \tag{1.1}$$

where $\mathbf{\Phi}$ is the modal matrix, containing both structural modes and control surface modes; $\Delta\mathbf{f}_A$ is the unsteady aerodynamic disturbance vector calculated by the surface doublet lattice method, which includes the aerodynamic force due to structural elastic vibrations $\Delta\mathbf{f}_{Ae}$, control surface deflections $\Delta\mathbf{f}_{A\delta}$, and gust disturbances $\Delta\mathbf{f}_{Ag}$; q_∞ is the dynamic pressure, $\mathbf{Q}(ik)$ is the generalized unsteady aerodynamic influence coefficient matrix with respect to the reduced frequency k; $\mathbf{q}_e$ is the modal coordinate vector, containing n modes; $\mathbf{\delta}$ is the control surface deflection vector, containing mm control surfaces; $\mathbf{w}_g$ is the gust intensity vector. When addressing large deformation problems, the linearized modes around the equilibrium position of static deformation are chosen as structural modes. According to the minimum state method, the rational function approximation (RFA) of unsteady aerodynamic forces is given by:

$$\mathbf{Q}(s) = \mathbf{A}_0 + \frac{b}{V_\infty}\mathbf{A}_1 s + \frac{b^2}{V_\infty^2}\mathbf{A}_2 s^2 + \mathbf{D}_s(\mathbf{I}_r s - \frac{V_\infty}{b}\mathbf{R}_a)^{-1}\mathbf{E}_s s \tag{1.2}$$

where s is the Laplace variable, b is the reference semi-chord length, V_∞ is the freestream velocity, and $\mathbf{A}_n (n=1,2,3)$, $\mathbf{D}_s$, and $\mathbf{E}_s$ are the polynomial coefficient matrices; $\mathbf{I}_r$ is the identity matrix of the same order as $\mathbf{R}_a$; $\mathbf{R}_a$ is the aerodynamic lag root matrix, containing tt aerodynamic lag roots. The matrices $\mathbf{E}_s$ and $\mathbf{A}_n (n=1,2,3)$ can be written as block matrices:

$$\mathbf{A}_n = [\mathbf{A}_{en} \quad \mathbf{A}_{\delta n} \quad \mathbf{A}_{gn}], \mathbf{E}_s = [\mathbf{E}_e \quad \mathbf{E}_\delta \quad \mathbf{E}_g] \quad (n=0,1,2) \tag{1.3}$$

Thus, the rational function approximations for the unsteady aerodynamic forces due to structural vibrations, control surface deflections, and gust disturbances can be expressed as:

$$\mathbf{Q}_e(s) = \mathbf{A}_{e0} + \frac{b}{V_\infty}\mathbf{A}_{e1}s + \frac{b^2}{V_\infty^2}\mathbf{A}_{e2}s^2 + \mathbf{D}_s(\mathbf{I}_r s - \frac{V_\infty}{b}\mathbf{R}_a)^{-1}\mathbf{E}_e s \tag{1.4}$$

$$\mathbf{Q}_\delta(s) = \mathbf{A}_{\delta0} + \frac{b}{V_\infty}\mathbf{A}_{\delta1}s + \frac{b^2}{V_\infty^2}\mathbf{A}_{\delta2}s^2 + \mathbf{D}_s(\mathbf{I}_r s - \frac{V_\infty}{b}\mathbf{R}_a)^{-1}\mathbf{E}_\delta s \tag{1.5}$$

$$\mathbf{Q}_g(s) = \mathbf{A}_{g0} + \frac{b}{V_\infty}\mathbf{A}_{g1}s + \frac{b^2}{V_\infty^2}\mathbf{A}_{g2}s^2 + \mathbf{D}_s(\mathbf{I}_r s - \frac{V_\infty}{b}\mathbf{R}_a)^{-1}\mathbf{E}_g s \tag{1.6}$$

Introducing the aerodynamic state variable:

$$\mathbf{x}_a(s) = (\mathbf{I}_r s - \frac{V_\infty}{b}\mathbf{R}_a)^{-1}\mathbf{E}_s s \begin{Bmatrix} \mathbf{q}_A(s) \\ \boldsymbol{\delta}(s) \\ \mathbf{w}_g(s) \end{Bmatrix}$$

$$= (\mathbf{I}_r s - \frac{V_\infty}{b}\mathbf{R}_a)^{-1}(\mathbf{E}_A s\mathbf{q}_A(s) + \mathbf{E}_\delta s\boldsymbol{\delta}(s) + \mathbf{E}_g s\mathbf{w}_g(s)) \tag{1.7}$$

Applying the inverse Laplace transform to the above equation:

$$\dot{\mathbf{x}}_a(t) = \mathbf{E}_A\dot{\mathbf{q}}_A(t) + \mathbf{E}_\delta\dot{\boldsymbol{\delta}}(t) + \mathbf{E}_g\dot{\mathbf{w}}_g(t) + \frac{V_\infty}{b}\mathbf{R}_a\mathbf{x}_a(t) \tag{1.8}$$

Substituting equations (1.2)(1.7)(1.8) into equation (1.1), we obtain the time-domain expression for the generalized unsteady aerodynamic force:

$$\boldsymbol{\Phi}\Delta\mathbf{f}_A = q_\infty[(\mathbf{A}_{A0}\mathbf{q}_A + \mathbf{A}_{\delta0}\boldsymbol{\delta} + \mathbf{A}_{g0}\mathbf{w}_g) + \frac{b}{V_\infty}(\mathbf{A}_{A1}\dot{\mathbf{q}}_A + \mathbf{A}_{\delta1}\dot{\boldsymbol{\delta}} + \mathbf{A}_{g1}\dot{\mathbf{w}}_g)$$

$$+ \frac{b^2}{V_\infty^2}(\mathbf{A}_{A2}\ddot{\mathbf{q}}_A + \mathbf{A}_{\delta2}\ddot{\boldsymbol{\delta}}) + \mathbf{D}_s\mathbf{x}_a] \tag{1.9}$$

It should be noted that when performing the rational function approximation of unsteady aerodynamic forces caused by gusts, $\mathbf{A}_{g2} = 0$.

3.2.2 Aeroservoelastic model for flexible aircraft

First, a nonlinear static aeroelastic analysis is performed. An aerodynamic model using the unsteady surface doublet lattice method is established based on the converged static deformation equilibrium configuration. By combining the current geometrically precise boundary conditions and flow field velocity, the unsteady aerodynamic loads at that moment are obtained using the unsteady surface doublet lattice method. The aerodynamic loads are interpolated and fixed in magnitude, then applied to the structure in the form of dynamic loading. Using a nonlinear reduced-order structural model, a transient analysis is performed to obtain new displacements and velocities. These displacements and velocities are then interpolated to update the aerodynamic surface positions and flow field boundary conditions for the next time step's unsteady aerodynamic load calculation. The displacements and velocities obtained from the transient analysis at each time

step serve as the initial conditions and boundary conditions for the structural analysis of the next time step, ensuring the continuity of the time-domain calculations. When the time step is sufficiently small, this algorithm can meet the required accuracy. The specific process for the gust response analysis method of large flexible wings based on the nonlinear reduced-order structural model is shown in Figure 6.
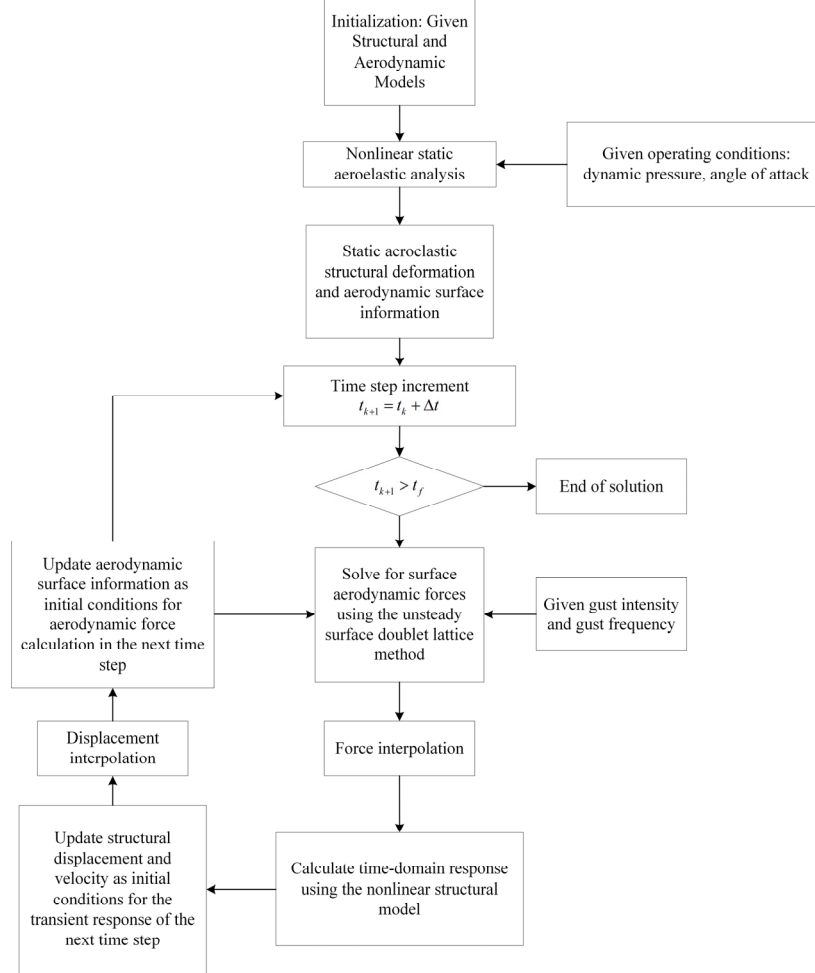

Figure 6 Flowchart of Gust Response Analysis for Large Flexible Wing

After dynamic linearization at the static deformation equilibrium position, the stiffness characteristics of the structure can be described by the tangent stiffness matrix, yielding the general time-domain equation of motion for an elastic aircraft:

$$\begin{bmatrix} \mathbf{M}_{qq} & \mathbf{M}_{q\delta} \end{bmatrix} \begin{Bmatrix} \ddot{\mathbf{q}}_e \\ \ddot{\boldsymbol{\delta}} \end{Bmatrix} + \begin{bmatrix} \mathbf{K}_{qT} & 0 \end{bmatrix} \begin{Bmatrix} \mathbf{q}_e \\ \boldsymbol{\delta} \end{Bmatrix} = \frac{1}{2}\rho V^2 \begin{bmatrix} \mathbf{Q}_{eT} & \mathbf{Q}_{\delta} \end{bmatrix} \begin{Bmatrix} \mathbf{q}_e \\ \boldsymbol{\delta} \end{Bmatrix} + \frac{1}{2}\rho V^2 \mathbf{Q}_g \mathbf{w}_g \qquad (1.10)$$

where $\mathbf{M}_{qq}$ is the generalized mass matrix of the structure, $\mathbf{M}_{q\delta}$ is the generalized mass matrix for the coupling between the structure and control surfaces, $\mathbf{K}_{qT}$ is the tangent stiffness matrix, and $\mathbf{Q}_{eT}$ represents the unsteady aerodynamic forces calculated based on the linearized modes at the static deformation equilibrium position. Combining equations (1.4) to (1.10), the state-space equations for the aeroelastic system are obtained:

$$\dot{\mathbf{x}}_S = \mathbf{A}_S \mathbf{x}_S + \mathbf{B}_S \mathbf{u}_S + \mathbf{B}_{Sg} \mathbf{u}_g \tag{1.11}$$

$$\mathbf{A}_S = \begin{bmatrix} \mathbf{0}_{(n \times n)} & \mathbf{I}_{(n \times n)} & \mathbf{0}_{(n \times t)} \\ \bar{\mathbf{M}}_q^{-1} \bar{\mathbf{K}}_T & \mathbf{0}_{(n \times n)} & \frac{1}{2} \rho V_\infty^2 \bar{\mathbf{M}}_q^{-1} \mathbf{D}_s \\ \mathbf{0}_{(t \times n)} & \mathbf{E}_e & \frac{V_\infty}{b} \mathbf{R}_a \end{bmatrix}$$

$$\mathbf{B}_S = \begin{bmatrix} \mathbf{0}_{(n \times m)} & \mathbf{0}_{(n \times m)} & \mathbf{0}_{(n \times m)} \\ \frac{1}{2} \rho V_\infty^2 \bar{\mathbf{M}}_q^{-1} \mathbf{Q}_{\delta 0} & \frac{1}{2} \rho V b \bar{\mathbf{M}}_q^{-1} \mathbf{Q}_{\delta 1} & \frac{1}{2} \rho b^2 \bar{\mathbf{M}}_\delta^{-1} \mathbf{Q}_{\delta 2} \\ \mathbf{0}_{(t \times m)} & \mathbf{E}_\delta & \mathbf{0}_{(t \times m)} \end{bmatrix}$$

$$\mathbf{B}_{Sg} = \begin{bmatrix} \mathbf{0}_{(1 \times l)} & \mathbf{0}_{(1 \times l)} \\ \frac{1}{2} \rho V_\circ \bar{\mathbf{M}}_q^{-1} \mathbf{Q}_{g 0} & \frac{1}{2} \rho b \bar{\mathbf{M}}_q^{-1} \mathbf{Q}_{g 1} \\ \mathbf{0}_{(1 \times l)} & \frac{\mathbf{E}_g}{V_\circ} \end{bmatrix}$$

$$\mathbf{x}_S = \begin{Bmatrix} \mathbf{q}_e \\ \dot{\mathbf{q}}_e \\ \mathbf{x}_a \end{Bmatrix}, \mathbf{u}_S = \begin{Bmatrix} \boldsymbol{\delta} \\ \dot{\boldsymbol{\delta}} \\ \ddot{\boldsymbol{\delta}} \end{Bmatrix}, \mathbf{u}_g = \begin{Bmatrix} \mathbf{w}_g \\ \dot{\mathbf{w}}_g \end{Bmatrix}$$

where:

$$\bar{\mathbf{M}}_q = \mathbf{M}_{qq} - \frac{1}{2} \rho b^2 \mathbf{Q}_{eT2}$$

$$\bar{\mathbf{K}}_T = \frac{1}{2} \rho V^2 \mathbf{Q}_{eT0} - \mathbf{K}_{qT}$$

$$\bar{\mathbf{M}}_\delta = \frac{1}{2} \rho b^2 \mathbf{Q}_{\delta 2} - \mathbf{M}_{q\delta}$$

The output equation expression depends on which physical quantity is chosen as the output, related to the signals measured by the sensors. When the acceleration at a certain point on the wing structure is chosen as the output physical quantity, the system output equation can be expressed as:

$$\mathbf{y}_S = \mathbf{C}_S \mathbf{x}_S + \mathbf{D}_S \mathbf{u}_S + \mathbf{D}_{Sg} \mathbf{u}_g \tag{1.12}$$

$$\mathbf{C}_S = \begin{bmatrix} \mathbf{\Phi}_p \bar{\mathbf{M}}_q^{-1} \bar{\mathbf{K}}_T & \mathbf{0}_{(p \times n)} & \dfrac{1}{2} \rho V^2 \mathbf{\Phi}_p \bar{\mathbf{M}}_q^{-1} \mathbf{D}_s \end{bmatrix}$$

$$\mathbf{D}_S = \begin{bmatrix} \dfrac{1}{2} \rho V_\infty^2 \mathbf{\Phi}_p \bar{\mathbf{M}}_q^{-1} \mathbf{Q}_{\delta 0} & \dfrac{1}{2} \rho V_\infty b \mathbf{\Phi}_p \bar{\mathbf{M}}_q^{-1} \mathbf{Q}_{\delta 1} & \dfrac{1}{2} \rho b^2 \mathbf{\Phi}_p \bar{\mathbf{M}}_\delta^{-1} \mathbf{Q}_{\delta 2} \end{bmatrix}$$

$$\mathbf{D}_{Sg} = \begin{bmatrix} \dfrac{1}{2} \rho V_\infty \mathbf{\Phi}_p \bar{\mathbf{M}}_q^{-1} \mathbf{Q}_{g0} & \dfrac{1}{2} \rho b \mathbf{\Phi}_p \bar{\mathbf{M}}_q^{-1} \mathbf{Q}_{g1} \end{bmatrix}$$

where $\mathbf{\Phi}_p$ is the modal matrix at a certain point on the structure, and p is the sensor measurement degrees of freedom. When the bending moment at a certain point on the wing structure is chosen as the output physical quantity, the system output equation can be expressed as:

$$\mathbf{y}_S = \mathbf{C}_S \mathbf{x}_S \tag{1.13}$$

$$\mathbf{C}_S = \begin{bmatrix} \bar{\mathbf{K}}_b & \mathbf{0}_{(1 \times n)} & \mathbf{0}_{(1 \times t)} \end{bmatrix}$$

where $\bar{\mathbf{K}}_b$ is the bending moment coefficient matrix obtained from the physical stiffness matrix of the structure.

3.2.3 Actuator and sensors modeling

The actuator segment is the executing mechanism of the servo control system, converting control command signals into control surface movements that produce control forces. Typically, the actuator is considered to be composed of a second-order servomechanism and a first-order booster, with corresponding nonlinear factors ignored. The transfer function of the actuator can generally be described using a third-order rational function:

$$\frac{\delta(s)}{u_c(s)} = \frac{b_0}{s^3 + a_2 s^2 + a_1 s + a_0} \tag{1.14}$$

where δ is the control surface deflection angle, and u_c is the actuator input voltage. Choosing $\mathbf{x}_{ac} = \begin{bmatrix} \delta & \dot{\delta} & \ddot{\delta} \end{bmatrix}^T$ as the state variable and $\mathbf{y}_{ac} = \begin{bmatrix} \delta & \dot{\delta} & \ddot{\delta} \end{bmatrix}^T$ as the output variable, the above equation can be written in the form of state-space equations:

$$\begin{aligned} \dot{\mathbf{x}}_{ac} &= \mathbf{A}_{ac} \mathbf{x}_{ac} + \mathbf{B}_{ac} \mathbf{u}_{ac} \\ \mathbf{y}_{ac} &= \mathbf{C}_{ac} \mathbf{x}_{ac} \end{aligned} \tag{1.15}$$

where $\mathbf{A}_{ac} = \begin{pmatrix} 0 & 1 & 0 \\ 0 & 0 & 1 \\ -a_0 & -a_1 & -a_2 \end{pmatrix}$ is the actuator characteristic matrix, and $\mathbf{B}_{ac} = \begin{bmatrix} 0 & 0 & b_0 \end{bmatrix}^T$ is the input coefficient matrix, $\mathbf{C}_a = I_{3 \times 3}$. Sensors, the sensitive elements in the servo system, are typically accelerometers, angular accelerometers, or strain gauges placed on the aircraft structure to detect the motion and load conditions of the elastic body. Generally, the sensor bandwidth is high enough compared to the modal frequencies of the aircraft structure, allowing sensors to be approximated as pure proportional gains without separate mathematical models. In this paper, sensors are also treated as ideal components.

3.2.4 Control laws modeling

A typical flight control law system consists of filters, integrators, delays, and gain systems. Similar to actuators and sensors, control law systems are often represented as a combination of subsystems in series or parallel. Thus, through appropriate state variable selection, the control law system can be modeled in the state-space form:

$$\dot{\mathbf{x}}_c = \mathbf{A}_c \mathbf{x}_c + \mathbf{B}_c \mathbf{u}_c$$
$$\mathbf{y}_c = \mathbf{C}_c \mathbf{x}_c + \mathbf{D}_c \mathbf{u}_c$$

(1.16)

where:

$$\mathbf{u}_c = \mathbf{y}_s$$
$$\mathbf{y}_c = \mathbf{u}_{ac}$$

(1.17)

3.2.5 Synthesized modeling for gust alleviation analysis

After establishing the open-loop state-space model of the system and introducing the control law design method and actuator segment, this section presents the gust alleviation control scheme for large flexible wings, obtaining the closed-loop system state-space model. Figure 70 shows the block diagram of the gust alleviation control scheme. For discrete gusts, the wingtip vertical acceleration is chosen as the feedback signal. The accelerometer signal is processed through a low-pass filter and fed back to the controller to obtain the actuator input signal, which commands the actuator to deflect and drive the control surface to achieve gust alleviation control for the large flexible wing.

Combining equations (1.11), (1.12), (1.13), (1.16) and setting $\mathbf{u}_s = \mathbf{y}_{ac}$, the open-loop system state-space equations can be derived:

$$\dot{\mathbf{x}}_a = \mathbf{A}_a \mathbf{x}_a + \mathbf{B}_a \mathbf{u}_{ac} + \mathbf{B}_g \mathbf{u}_g$$
$$\mathbf{y}_S = \mathbf{C}_a \mathbf{x}_a + \mathbf{D}_{Sg} \mathbf{u}_g$$

(1.18)

where:

$$\mathbf{x}_a^T = \left\{ \mathbf{x}_S^T \quad \mathbf{x}_{ac}^T \right\}$$

$$\mathbf{A}_a = \begin{pmatrix} \mathbf{A}_S & \mathbf{B}_S \mathbf{C}_{ac} \\ \mathbf{0} & \mathbf{A}_{ac} \end{pmatrix}, \mathbf{B}_a = \begin{bmatrix} \mathbf{0} \\ \mathbf{B}_{ac} \end{bmatrix}, \mathbf{B}_g = \begin{bmatrix} \mathbf{B}_{Sg} \\ \mathbf{0} \end{bmatrix}, \mathbf{C}_a = \begin{bmatrix} \mathbf{C}_S & \mathbf{D}_S \mathbf{C}_{ac} \end{bmatrix}$$

Combining equations (1.16)(1.17)(1.18), the state-space equations for the closed-loop gust alleviation system are obtained:

$$\begin{Bmatrix} \dot{\mathbf{x}}_a \\ \dot{\mathbf{x}}_k \end{Bmatrix} = \begin{pmatrix} \mathbf{A}_a + \mathbf{B}_a \mathbf{D}_k \mathbf{C}_a & \mathbf{B}_a \mathbf{C}_k \\ \mathbf{B}_k \mathbf{C}_a & \mathbf{A}_k \end{pmatrix} \begin{Bmatrix} \mathbf{x}_a \\ \mathbf{x}_k \end{Bmatrix} + \begin{bmatrix} \mathbf{B}_g \\ \mathbf{0} \end{bmatrix} \mathbf{u}_g$$

$$\mathbf{y}_S = \begin{bmatrix} \mathbf{C}_a & \mathbf{0} \end{bmatrix} \begin{Bmatrix} \mathbf{x}_a \\ \mathbf{x}_k \end{Bmatrix} + \mathbf{D}_{S_g} \mathbf{u}_g$$

(1.19)

Based on equations (1.18) and (1.19), the open-loop and closed-loop responses of the system can be provided under specified control parameters to verify the effectiveness of the gust alleviation control law design. It is crucial to emphasize that the gust alleviation control is based on the

dynamic linearization of the wing system at the static deformation equilibrium position. The structural stiffness matrices involved in the system matrices are all tangent stiffness matrices obtained from the reduced-order structural model, and the aerodynamic coefficient matrices are all solved based on the linearized modal information at the static deformation equilibrium position.

4   AEROSERVOELASTIC ANALYSIS

4.1   Nonlinear Static Aeroelastic Iteration Results

Figures 7 and 8 respectively illustrate the nonlinear static aeroelastic iteration results for the single and dual aircraft configurations. Subsequent research will be based on these large deformation states to further conduct analysis.
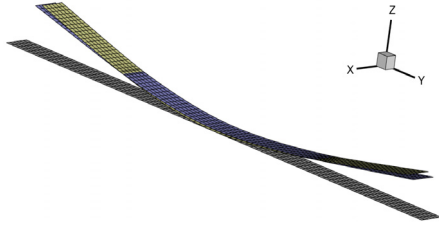
Figure 7 Single Aircraft
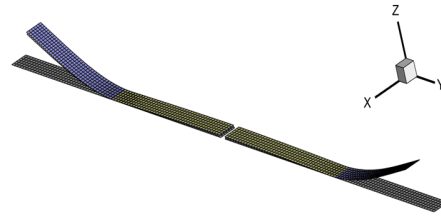
Figure 8 Dual Aircraft

4.2   Gust alleviation for discrete gust excitation

Based on the nonlinear static aeroelastic deformation obtained in the preliminary analysis, research on gust alleviation control considering geometric nonlinearity is carried out.

This paper employs a 1-cosine discrete gust model, with the mathematical expression given by equation (1.20):

$$
\begin{cases}
w_g(x) = 0 & x < 0 \\
w_g(x) = \dfrac{w_{gm}}{2}(1 - \cos\dfrac{2\pi x}{L_g}) & 0 \le x \le L_g \\
w_g(x) = 0 & x < L_g
\end{cases}
\tag{1.20}
$$

During the simulation of gust alleviation control for the wing, the control surface is set at a distance of 500mm from the wing root, with an average aerodynamic chord length of 30mm and a control surface area of 10800 square millimeters. The actuator linkages are specified as ideal actuator linkages. The evaluation of the gust alleviation system's effectiveness is described in terms of gust load alleviation rate, expressed as follows:

$$
\eta = \frac{a_{open} - a_{close}}{a_{open}} \times 100\%
\tag{1.21}
$$

In which, a_{open} represents the maximum output response peak in the open-loop frequency response analysis, and a_{close} represents the maximum output response peak in the closed-loop frequency response analysis. Gust alleviation simulation analysis is conducted in MATLAB, and the Simulink simulation diagram of the wind gust alleviation system is shown in Figure 9.
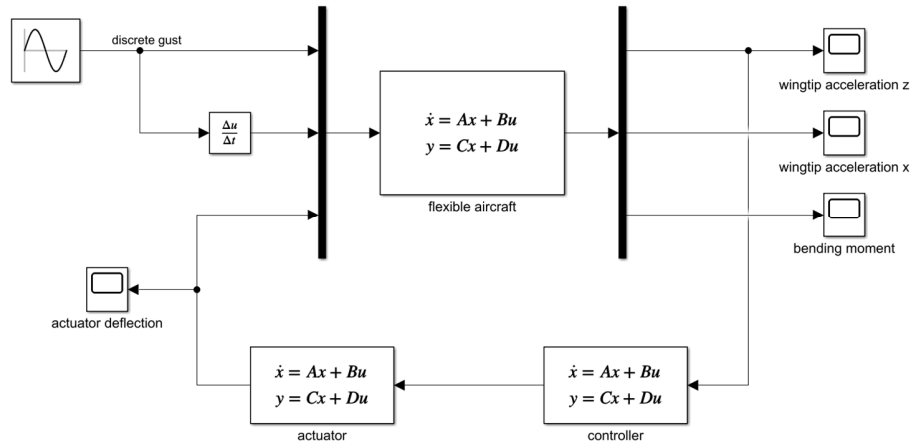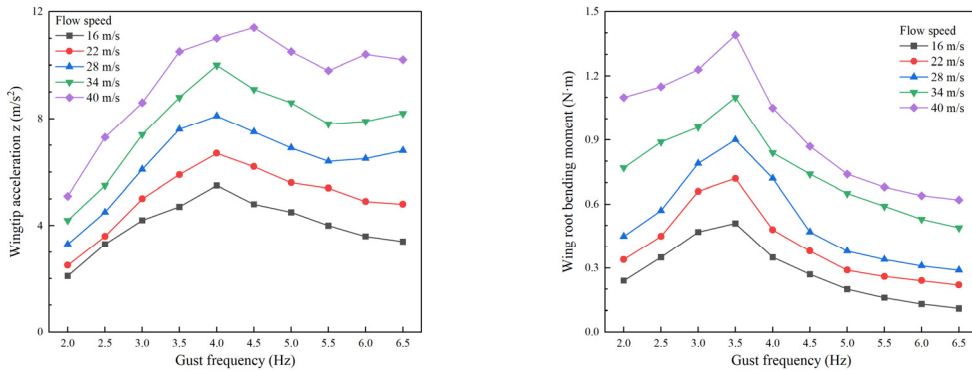
Figure 9 SIMULINK model of gust load alleviation controller architecture

（**a**）Wingtip acceleration response　　（**b**）Wing root bending moment response

Figure 10 Open-loop gust response results

Figure 10 shows the open-loop response graphs of wingtip z-direction acceleration and wing root bending moment under different conditions. It can be seen that as the inflow speed increases, the amplitude of the gust response gradually increases, and the subject of this study is particularly sensitive at a gust frequency of 3.5Hz. Figure 11 presents the simulation analysis results of the time-domain response of a large flexible composite aircraft under wind speed of 28m/s and gust frequency of 2.5Hz, for both open-loop and closed-loop scenarios. The control system demonstrates a significant suppression effect on wingtip acceleration response and wing root bending moment load response, indicating the rational and effective nature of the gust alleviation control strategy. The designed control scheme can simultaneously alleviate wingtip vertical acceleration and wing root bending moment load, with alleviation rates exceeding 45% for both.
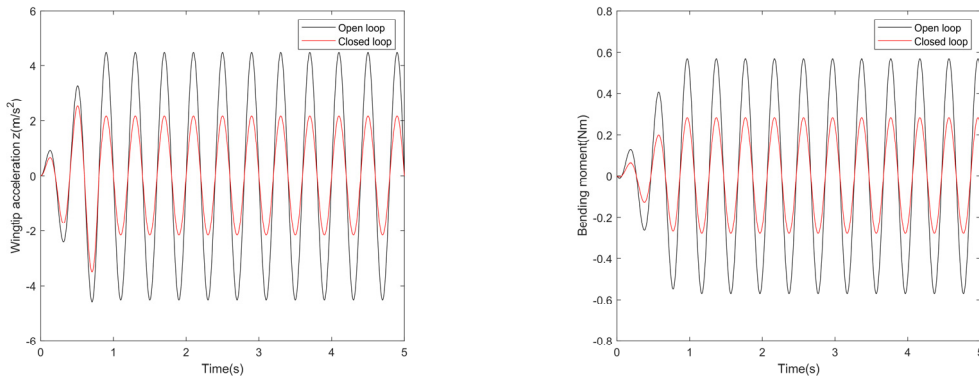
（**a**）Wingtip acceleration response （**b**）Wing root bending moment response
Figure 11 Simulation results of gust alleviation at speed 28m/s and gust frequency 2.5Hz

5　CONCLUSIONS

1）The state-space equations for gust alleviation have been established, providing a reference for future research on new control methods.

2）Aeroservoelastic analysis of large aspect ratio flexible composite aircraft must account for geometric nonlinearities, which affect subsequent control law designs.

3）The control method studied in this paper achieves gust alleviation rates of over 45%, effectively ensuring the aerodynamic servoelastic stability of the aircraft.

REFERENCES

[1]　Shafaghat S, Noorian M A, Irani S. Nonlinear aeroelastic analysis of a HALE aircraft with flexible components[J]. Aerospace Science and Technology, 2022, 127: 107663.

[2]　He C, Zhan F, Ma L, et al.. Aero-structural design of joined-wing aircraft based on high-fidelity model[J]. Chinese Journal of Aeronautics, 2024, 37(4): 363–377.

[3]　Cobar M, Montalvo C. Takeoff and Landing of a Wing-Tip-Connected Meta Aircraft with Feedback Control[J]. Journal of Aircraft, 2021, 58(4): 733–742.

[4]　Montalvo C, Costello M. Meta Aircraft Flight Dynamics[J]. Journal of Aircraft, 2015, 52(1): 107–115.

[5]　Montalvo C, Costello M. Meta Aircraft Connection Dynamics[A]. AIAA Guidance, Navigation, and Control Conference[C]. Minneapolis, Minnesota: American Institute of Aeronautics and Astronautics, 2012.

[6]　Köthe A, Behrens A, Hamann A, et al.. Closed-loop flight tests with an unmanned experimental multi-body aircraft[A]. International Forum on Aeroelasticity and Structural Dynamics (IFASD)[C]. Curran Assoc. New York, 2017: 25–28.

[7]　Meng Y, An C, Xie C, et al.. Conceptual design and flight test of two wingtip-docked multi-body aircraft[J]. Chinese Journal of Aeronautics, 2022, 35(12): 144–155.

[8] An C, Wang L, Xie C, et al.. Aerodynamics Characteristics and Flight Dynamics Analysis of Multi-body Aircraft[A]. 见: S. Lee, C. Han, J.-Y. Choi, et al.. The Proceedings of the 2021 Asia-Pacific International Symposium on Aerospace Technology (APISAT 2021), Volume 1[M]. Singapore: Springer Nature Singapore, 2023, 912: 375–384.

[9] Drew M C, Hashemi K E, Cramer N B, et al.. Multi-Objective Gust Load Alleviation Control Designs for an Aeroelastic Wind Tunnel Demonstration Wing[A]. AIAA Scitech 2020 Forum[C]. Orlando, FL: American Institute of Aeronautics and Astronautics, 2020.

[10] Hashemi K E, Nguyen N T, Drew M C, et al.. Performance Optimizing Gust Load Alleviation Control of Flexible Wing Aircraft[A]. 2018 AIAA Guidance, Navigation, and Control Conference[C]. Kissimmee, Florida: American Institute of Aeronautics and Astronautics, 2018.

[11] Wang X, Van Kampen E, Chu Q P, et al.. Flexible Aircraft Gust Load Alleviation with Incremental Nonlinear Dynamic Inversion[J]. Journal of Guidance, Control, and Dynamics, 2019, 42(7): 1519–1536.

[12] Vindigni C R, Orlando C. Simple adaptive V-stack piezoelectric based airfoil flutter suppression system[J]. Journal of Vibration and Control, 2023, 29(11–12): 2802–2816.

[13] Zhou Y, Wu Z, Yang C. Intelligent feedforward gust alleviation based on neural network[J]. Chinese Journal of Aeronautics, 2024, 37(3): 116–132.

COPYRIGHT STATEMENT